

# Probing atom-surface interactions by diffraction of Bose-Einstein condensates

Helmar Bender, Christian Stehle, Claus Zimmermann, and Sebastian Slama\*  
*Physikalisches Institut and Center for Collective Quantum Phenomena in LISA+,  
Universität Tübingen, Auf der Morgenstelle 14, D-72076 Tübingen, Germany*

Johannes Fiedler and Stefan Scheel  
*Institut für Physik, Universität Rostock, Universitätsplatz 3, D-18055 Rostock, Germany*

Stefan Yoshi Buhmann†  
*Quantum Optics and Laser Science, Blackett Laboratory, Imperial College London,  
Prince Consort Road, London SW7 2AZ, United Kingdom*

Valery N. Marachevsky‡  
*Institute of Theoretical and Mathematical Physics,  
Saint-Petersburg State University, 198504 St.Petersburg, Russia*  
(Dated: November 27, 2024)

In this article we analyze the Casimir–Polder interaction of atoms with a solid grating and an additional repulsive interaction between the atoms and the grating in the presence of an external laser source. The combined potential landscape above the solid body is probed locally by diffraction of Bose-Einstein condensates. Measured diffraction efficiencies reveal information about the shape of the Casimir–Polder interaction and allow us to discern between models based on a pairwise-summation (Hamaker) approach and Lifshitz theory.

PACS numbers: 03.75.Lm, 37.10.Vz, 42.50.Ct, 67.85.Hj

The Casimir–Polder (CP) interaction is one of a class of examples where fluctuating electromagnetic fields give rise to (normally attractive) forces between matter [1, 2]. For infinitely extended plane surfaces CP forces can be readily calculated from the polarizability of the atom and the dielectric properties of the substrate [3] and have been measured in a number of experiments [4–9]. However, of particular importance is the influence of the surface geometry [10, 11]. Non-trivial geometries can have a large impact on the exact force profile and can potentially be used for manipulating the closely related Casimir forces [12]. The possibility to tailor the Casimir force is also of importance for applications in the MEMS and NEMS industry where it is one of the limiting factors in the miniaturization of micromachines and microsensors [13].

One class of non-trivial geometries that have been investigated theoretically both in the framework of atom-surface and surface-surface interactions are periodic structures such as gratings [14–16]. Experimentally, CP forces above gratings were measured by different methods [17–21]. In those experiments, the power law coefficients describing the CP potential in the electrostatic and in the retarded regimes were determined. However, the measured values represent only an average over the complicated potential landscape above the structures. In this work we fully account for the dependence of the potential on the lateral position above such a surface.

Dispersion potentials in nontrivial geometries can be calculated using the Hamaker approach [22, 23], which is based on a pairwise summation of van der Waals forces

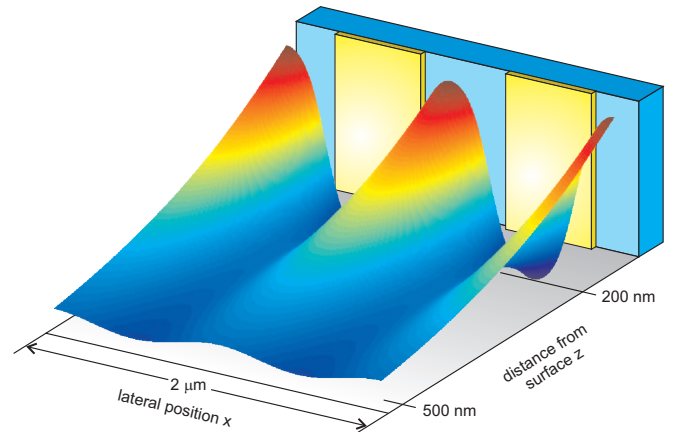


FIG. 1: Sketch of the metal grating including the combined Casimir-Polder and evanescent wave potential landscape as calculated from Eqs. (1) and (2) within Lifshitz theory for a laser power of  $P = 200$  mW. The distances from the surface range from  $z = 200$  nm to  $z = 500$  nm, the lateral position span is  $2 \mu\text{m}$  and the potential modulation at a distance of  $z = 200$  nm is  $\Delta E/k_B = 14 \mu\text{K}$ .

between volume elements of one body with those of the other. However, such an approach neglects many-body interactions which can lead to wrong results in particular for complex geometric structures [24, 25]. The non-additivity of Casimir forces induced by many-body interactions [26] implies that the position-, shape- and material-dependencies of such forces are intertwined in a complicated way. Nevertheless, the Hamaker approach

is widely used in applications such as colloid science and biology [27]. The most prominent example is the adhesive force of gecko feet [28]. Recently, experiments have shown deviations from Hamaker theory in surface-surface interactions [25]. Surprisingly, not a single experiment has so far addressed the accuracy of the Hamaker approach in atom-surface interactions.

In this Letter we present both simulations and measurements of the potential landscape for a single atom that is positioned at a submicron distance from a grating of metal nanowires (see Fig. 1). Our measurements allow us to distinguish between results obtained using the Hamaker approach and those using exact Lifshitz theory.

The potential landscape is composed of an attractive contribution due to the Casimir–Polder force and a repulsive contribution due to an evanescent light wave (EW) at the surface. The evanescent wave is generated by internal total reflection of a laser beam in the dielectric substrate carrying the grating. A repulsion from the surface is achieved by a laser ( $\lambda = 765$  nm) that is blue-detuned with respect to the transition frequency of the atoms (Rb:  $\lambda_0 = 780$  nm). Recently, we used this setup and enhanced the evanescent waves by exciting surface plasmon polaritons at the surface [29]. Here, we exploit the fact that the exact shape of the total potential landscape can be tuned by the strength of the optical dipole potential via the laser intensity. This allows us to acquire spatially resolved information on the potential landscape.

Figure 1 shows the calculated potential landscape in Lifshitz theory for a typical laser power of  $P = 200$  mW including the optical dipole potential of the evanescent wave. In the simulations, the ground-state CP potential of the atoms is calculated as [30]

$$U_{CP}(\mathbf{r}) = \frac{\hbar\mu_0}{2\pi} \int_0^\infty d\xi \xi^2 \alpha(i\xi) \text{Tr} \mathbf{G}^{(1)}(\mathbf{r}, \mathbf{r}, i\xi). \quad (1)$$

Here,  $\alpha(i\xi)$  is the isotropic ground-state polarisability of the Rb atoms and  $\mathbf{G}^{(1)}$  is the scattering Green tensor which, for the grating structure in Fig. 1, can be given as a Rayleigh decomposition. Due to the integral over all imaginary frequencies as a result of the vacuum fluctuations of the e.m. field, the CP potential depends on all atomic transition frequencies and all eigenfrequencies of the macroscopic system (grating).

The EW potential

$$U_{EW}(\mathbf{r}) = \sum_{i=1,2} \frac{|\mathbf{d}_i|^2 |\mathbf{E}(\mathbf{r})|^2}{3\hbar\Delta_i} \quad (2)$$

is the potential due to the external monochromatic electric field  $\mathbf{E}$  with its frequency  $\omega$  close a specific set of atomic transitions of Rb with dipole matrix elements  $\mathbf{d}_i$  and detunings  $\Delta_i = \omega - \omega_i$ . It is dominated by these atomic transitions and the transmission properties of the grating at a single laser frequency  $\omega$ .

In contrast, the CP potential in the Hamaker approach is calculated in local-field corrected first-order Born approximation as

$$\mathbf{G}^{(1)}(\mathbf{r}, \omega) = \frac{\omega^2}{c^2} \frac{\chi(\omega)}{1 + \chi(\omega)/3} \times \int d^3s \mathbf{R}^{(0)}(\mathbf{r}, \mathbf{s}, \omega) \mathbf{R}^{(0)}(\mathbf{s}, \mathbf{r}, \omega) \quad (3)$$

where  $\mathbf{R}^{(0)}(\mathbf{r}, \mathbf{s}, \omega)$  is the regular part of the Green tensor,  $\chi(\omega)$  is the susceptibility of the gold stripes, and the integration extends over the total volume  $V$  of the grating. Details of all the calculations are contained in [31].

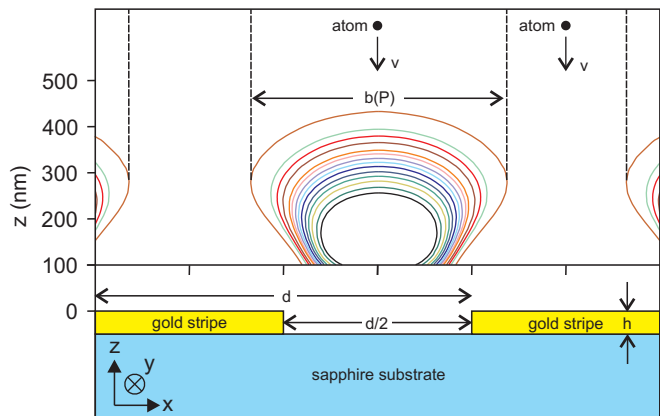


FIG. 2: Geometry of the metal grating. Approximately 200 gold stripes with  $h = 50$  nm height and 500 nm width are deposited on a sapphire substrate and form a grating with  $d = 1 \mu\text{m}$  period. The combination of the repulsive potential due to the evanescent wave with the Casimir–Polder interaction forms a potential landscape above the grating. The colored lines (black to brown, corresponding to laser powers  $P = 120, 126, 133, 138, 144, 151, 156, 162, 169, 174, 187, 198, 211, 247$  mW) are simulations of equipotential lines using Lifshitz theory for a  $^{87}\text{Rb}$  atom moving towards the surface with velocity  $v = 3.4$  cm/s. From those we deduce the width  $b(P)$  where atoms are reflected.

The CP potential with its strong attraction towards the gold stripes and the repulsive EW potential with its maximal repulsion above the sapphire surface combine to the periodic potential landscape in Fig. 1. It resembles a chain of hills in front of the grating surface with valleys that lead to the centers of the gold stripes. The heights and widths of the hills depend on the laser power (Fig. 2) with larger powers resulting in higher and broader hills. Experimentally, we probe the width of the hills by reflecting Bose–Einstein condensates (BEC) from the surface.

The experiment is carried out as follows. A BEC is prepared in a magnetic trap close to the surface of the grating and accelerated such that it moves towards the surface with a constant velocity  $v = 3.4$  cm/s. The experimental details of this preparation are contained in [31]. The atoms reflect from the surface only at those lateral positions where the potential height exceeds the kinetic

energy of the atoms. This happens in a zone with width  $b$  in each lattice site (see Fig. 2). Note that considerable quantum reflection of Rb atoms at the CP potential of a solid surface would require atomic velocities below few mm/s [7]. For the used velocity of  $v = 3.4$  cm/s it is completely negligible. By tuning the laser power, the reflection zone width  $b$  is changed and different distances from the surface are probed. Each atom of the BEC approaching the surface constitutes a matter wave with a lateral extension that is given by the size of the BEC on the order of several tens of microns. This size is much larger than the grating period, thus the matter wave is diffracted from the periodic structure of reflection zones in a direction  $x$  of period  $d$ .

In a simplified model that neglects the curvature of the equipotential lines we consider reflection of the matter wave from the same reflection zones of width  $b$  as for a single atom. The resulting atomic momentum distribution in the far field is analogous to Fraunhofer diffraction of light and is determined by the Fourier transform of the step function  $\sum_n \theta(b/2 - |x - nd|)$ . In this density imprinting model, the external potential leads to a reflection of the matter wave, but does not significantly alter its phase. For a periodic arrangement of rectangular stripes as shown in Fig. 2, the reflected wave is composed of wavevectors  $k_x$  with relative occupation  $p(k_x)$ ,

$$p(k_x) \propto \sum_n \delta(k_x - nq) \cdot \left| \text{sinc} \left( \frac{\pi k_x}{q} \cdot \frac{b}{d} \right) \right|^2. \quad (4)$$

This expression is a sum over delta functions at integer multiples  $n$  of the lattice vector  $q = 2\pi/d$ . The number  $n$  denotes the diffraction order. The sum is multiplied with an envelope amplitude given by a sinc-function that determines the corresponding occupation of the diffraction order. The relative occupation of the diffraction orders depends only on the ratio  $b/d$ . This is illustrated in the theoretical curves in Fig. 3. In the limit of  $b/d \rightarrow 0$  the situation resembles the emission of waves from a chain of point-like sources, in which all diffraction orders are equally occupied. In contrast, the limit  $b/d \rightarrow 1$  corresponds to a reflection from a surface with constant density profile. Here, the atomic cloud remains fully in the diffraction order  $n = 0$  with wavevector  $k_x = 0$ .

In the experiment, we analyze the relative occupation of individual diffraction orders by measuring the momentum distribution  $p_x = \hbar k_x$  of the atoms. This is done by taking an absorption image of the cloud after ballistic expansion for a time-of-flight of  $t_{\text{tof}} = 21.5$  ms after reflection from the surface. A typical image is shown in the inset of Fig. 3. From the image the atom numbers  $N_n$  corresponding to diffraction orders  $n$  are counted within the yellow boxes and are scaled to the total number of reflected atoms. This provides us data triples of relative populations of diffraction orders  $n = 0, \pm 1, \pm 2$  for each value of laser power. The populations for  $n \neq 0$

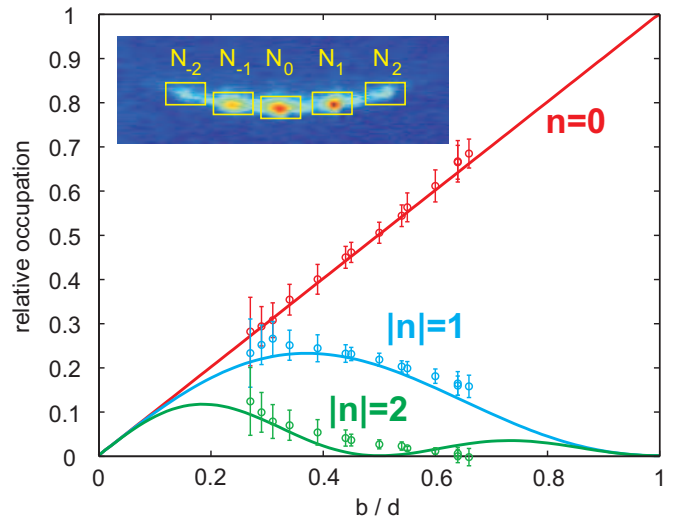


FIG. 3: Matter wave diffraction. Relative occupation of diffraction orders as a function of the relative width of the reflection zone  $b/d$ . The curves are obtained from Eq. (4). Data points represent the measured occupation of diffraction orders like shown in the inset. The horizontal position of each triple of data points (its value  $b/d$ ) is obtained from a fit to the theoretical curves.

are averaged over the populations of the orders with  $\pm n$ . Each triple is individually fitted by Eq. (4) and is thus attributed a certain value of  $b/d$ . The result of the fit is compared with the theoretical curves in Fig. 3. The fact that the data points coincide with the corresponding theory curves for each triple is a signature that the diffraction process is well described within the simple model.

The fitted values of  $b/d$  are now compared with the theoretical prediction which is accessible from the width of the equipotential lines shown in Fig. 2. As can be seen in Fig. 4, the experimental data agree with the Lifshitz theory within their statistic and systematic errors. In contrast, the Hamaker approach underestimates the strength of the Casimir-Polder potential. The corresponding values of  $b/d$  for low values of  $P$  in Fig. 4 are thus larger than the observed data points and deviate from them by more than one standard deviation. In the range of large  $P$  in Fig. 4 the optical potential dominates over the CP potential and reduces the difference between Lifshitz theory and Hamaker model. In this regime the data are compatible with both theoretical models.

The different functional profiles of the line shapes of the data points and the Lifshitz theory can be attributed to the simplicity of the diffraction model: in particular, the value of  $b/d$  of the measured data points saturates for large laser powers. This observation is not compatible with the density imprinting model. For high reflectivities an additional effect comes into play. Here, the assumption of instantaneous reflection is not justified. Instead, the interaction time of the atoms with the surface potential and the strength of the latter depend on the lateral

position  $x$ , i.e. depending on the lateral position the matter wave acquires a different phase. A periodic potential imprints a phase that leads to a substantial diffraction even when all atoms are reflected and thus simulates a saturation of  $b/d$  even for large laser powers [32, 33].

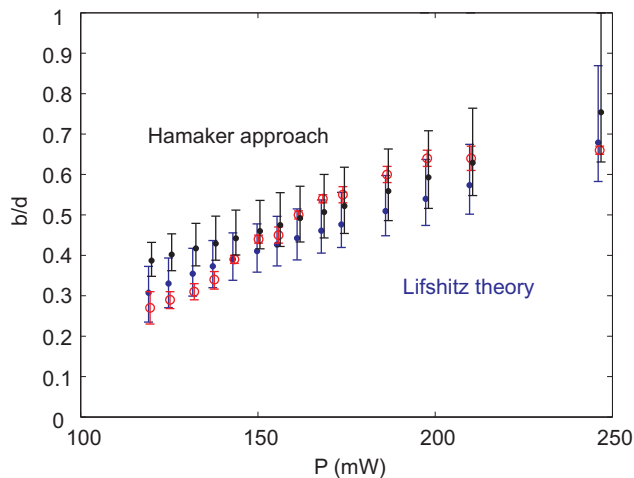


FIG. 4: Comparison between theory and experiment. Width of the reflection zone  $b/d$  versus laser power  $P$ . Red circles are experimental data points obtained from the fit in Fig. 3. Error bars of the data points are due to the combined statistic and systematic uncertainty in the atom number measurement. Blue dots show the theoretical values taken from the equipotential lines in Fig. 2 and represent the result of the Lifshitz model. Black points are the corresponding results based on a Hamaker approach. Error bars of the theoretical points represent the systematic error due to the uncertainty in the laser intensity at the surface  $\Delta I = \pm 5\%$  and the velocity of the atoms  $\Delta v = \pm 0.3$  cm/s. Please note that the data points are horizontally shifted one line width ( $\lesssim 1$  mW) for clarity.

Concluding, we have experimentally probed surface potential landscapes that are composed of Casimir–Polder forces and optical dipole forces above metallic nanostructures. We have used matter-wave diffraction of Bose-Einstein condensates as a measuring tool which, in principle, can be applied to arbitrary surfaces. Complementary to previous experiments in which spatial averages of the Casimir–Polder coefficients were determined, we obtain additional spatial information by analyzing the occupation of individual diffraction orders. Our data agree quantitatively with numerical calculations of the surface potentials based on Lifshitz theory, whereas a Hamaker approach leads to incompatible results for low laser powers.

The fact that we understand these potentials very well is crucial for the design and realization of nanoscale surface traps for surface quantum optics experiments with cold atoms. Moreover, the metallic parts of the surface can give rise to spectrally broad surface plasmon resonances in the optical frequency range. Related phonon polariton resonances in the infrared frequency range have e.g. led to the observation of repulsive Casimir–Polder

forces of highly excited Cs atoms [34]. A plasmon-based repulsive Casimir–Polder force would offer fascinating scenarios for controlling CP forces [35] and for generating surface traps for cold atoms that do not require external magnetic or optical fields.

C.S. was supported by Carl-Zeiss Stiftung Baden-Württemberg. Support from the European Science Foundation (ESF) within the activity ‘New Trends and Applications of the Casimir Effect’ is gratefully acknowledged. This work was financially supported by the UK EPSRC and by the COSCALI network within the IRSES program of the European Commission under Grant No. PIRSES-GA-2010-268717. V.N.M was partially supported by the Saint-Petersburg State University grant No 11.38.660.2013. Furthermore, we acknowledge support by the Deutsche Forschungsgemeinschaft within the European Collaborative Research program of the European Science Foundation.

\* Electronic address: slama@pit.physik.uni-tuebingen.de

† Electronic address: s.buhmann@imperial.ac.uk

‡ Electronic address: maraval@mail.ru

- [1] J.E. Lennard Jones, *Trans. Far. Soc.* **28**, 333 (1932).
- [2] H.B.G. Casimir and D. Polder, *Phys. Rev.* **73**, 360 (1948).
- [3] S. Scheel and S.Y. Buhmann, *Acta Phys. Slov.* **58**, 675 (2008).
- [4] C.I. Sukenik, M.G. Boshier, D. Cho, V. Sandoghdar, and E.A. Hinds, *Phys. Rev. Lett.* **70**, 560 (1993).
- [5] F. Shimizu, *Phys. Rev. Lett.* **86**, 987 (2001).
- [6] V. Druzhinina and M. DeKieviet, *Phys. Rev. Lett.* **91**, 193202 (2003).
- [7] T.A. Pasquini *et al.*, *Phys. Rev. Lett.* **93**, 223201 (2004).
- [8] J.M. Obrecht *et al.*, *Phys. Rev. Lett.* **98**, 063201 (2007).
- [9] H. Bender, P.W. Courteille, C. Marzok, C. Zimmermann, and S. Slama, *Phys. Rev. Lett.* **104**, 083201 (2010).
- [10] A.W. Rodriguez, F. Capasso, and S.G. Johnson, *Nature Phot.* **5**, 211 (2011).
- [11] V.N. Marachevsky, *J. Phys. A: Math. Theor.* **45**, 374021 (2012).
- [12] M. Levin, A.P. McCauley, A.W. Rodriguez, M.T. Homer Reid, and S.G. Johnson, *Phys. Rev. Lett.* **105**, 090403 (2010).
- [13] F.W. DelRio *et al.*, *Nature Mater.* **4**, 629 (2005).
- [14] A. Lambrecht and V.N. Marachevsky, *Phys. Rev. Lett.* **101**, 160403 (2008).
- [15] A.M. Contreras-Reyes *et al.*, *Phys. Rev. A* **82**, 052517 (2010).
- [16] P.S. Davids, F. Intravaia, F.S.S. Rosa, and D.A.R. Dalvit, *Phys. Rev. A* **82**, 062111 (2010).
- [17] T.A. Pasquini *et al.*, *Phys. Rev. Lett.* **97**, 093201 (2006).
- [18] B.S. Zhao, S.A. Schulz, S.A. Meeck, G. Meijer, and W. Schöllkopf, *Phys. Rev. A* **78**, 010902(R) (2008).
- [19] R.E. Grisenti, W. Schöllkopf, J.P. Toennies, G.C. Hegerfeldt, and T. Köhler, *Phys. Rev. Lett.* **83**, 1755 (1999).
- [20] H. Oberst, D. Kouznetsov, K. Shimizu, J.I. Fujita, and F. Shimizu, *Phys. Rev. Lett.* **94**, 013203 (2005).

- [21] J.D. Perreault and A.D. Cronin, Phys. Rev. Lett. **95**, 133201 (2005).
- [22] J.H. de Boer, Trans. Faraday Soc. **32**, 10 (1936).
- [23] H.C. Hamaker, Physica IV **10**, 1058 (1937).
- [24] S.N. Thennadil and L.H. Garcia-Rubio, J. Colloid Interface Sci. **243**, 136 (2001).
- [25] H.-C. Chiu, G.L. Klimchitskaya, V.N. Marachevsky, V.M. Mostepanenko, and U. Mohideen, Phys. Rev. B **80**, 121402(R) (2009).
- [26] S.Y. Buhmann and D.-G. Welsch, Appl. Phys. B **82**, 189 (2006).
- [27] V. A. Parsegian, *Van der Waals Forces: A Handbook for Biologists, Chemists, Engineers, and Physicists* (Cambridge University Press, New York, 2005).
- [28] K. Autumn *et al.*, Nature **405**, 681 (2000).
- [29] C. Stehle *et al.*, Nature Phot. **5**, 494 (2011).
- [30] S.Y. Buhmann, L. Knöll, D.G. Welsch, and H.T. Dung, Phys. Rev. A **70**, 052117 (2004).
- [31] See Supplemental Material for details on the calculation of the potentials and for the BEC preparation.
- [32] A. Günther, S. Kraft, C. Zimmermann, and J. Fortágh, Phys. Rev. Lett. **98**, 140403 (2007).
- [33] A.D. Cronin, J. Schmiedmayer, and D.E. Pritchard, Rev. Mod. Phys. **81**, 1051 (2009).
- [34] H. Failache, S. Saltiel, M. Fichet, D. Bloch, and M. Ducloy, Phys. Rev. Lett. **83**, 5467 (1999).
- [35] F. Intravaia, C. Henkel, and A. Lambrecht, Phys. Rev. A **76**, 033820 (2007).

# Probing atom-surface interactions by diffraction of Bose-Einstein condensates

## Supplemental Material

### I. SIMULATION OF THE CASIMIR-POLDER POTENTIAL

The ground-state CP potential of an atom can be given as [1]

$$U_{\text{CP}}(\mathbf{r}) = \frac{\hbar\mu_0}{2\pi} \int_0^\infty d\xi \xi^2 \text{Tr}[\boldsymbol{\alpha}(i\xi) \cdot \mathbf{G}^{(1)}(\mathbf{r}, \mathbf{r}, i\xi)]. \quad (1)$$

Here,  $\boldsymbol{\alpha}(i\xi)$  is the ground-state polarisability tensor and  $\mathbf{G}^{(1)}$  is the scattering Green tensor. We are neglecting thermal contributions to the CP force, which is a good approximation for the distances considered in this work. For the structure in Fig. 2 in the paper, the latter can be given in a Rayleigh decomposition

$$\mathbf{G}^{(1)}(\mathbf{r}, \mathbf{r}', \omega) = \frac{i}{8\pi^2} \int_{-\pi/d}^{\pi/d} dk_x \sum_{m,n=-\infty}^{\infty} \int_{-\infty}^{\infty} dk_y \times \sum_{\sigma,\sigma'=E,H} \frac{e^{i(k_x^m x - k_x^n x') + i k_y(y - y') + i(k_z^{m+} z + k_z^{n-} z)}}{k_z^{n-}} e_{m+}^{\sigma}(k_x, k_y, \omega) R_{mn}^{\sigma\sigma'}(k_x, k_y, \omega) e_{n-}^{\sigma'}(k_x, k_y, \omega). \quad (2)$$

Here,  $\mathbf{k}_{\pm} = (k_x^m, k_y, k_z^{m\pm})$  is the wave vector for upward/downward moving waves; its  $x$ - and  $z$ -components read  $k_x^m = k_x + mq$  ( $q = 2\pi/d$ : lattice vector of the grating) and  $k_z^{m\pm} = \sqrt{\omega^2/c^2 - (k_x^m)^2 - k_y^2}$  with  $\text{Im } k_z^{m\pm} \geq 0$ ; and the polarisation unit vectors are defined by

$$\mathbf{e}_{m\pm}^E(k_x, k_y, \omega) = \frac{c}{\omega \sqrt{\omega^2/c^2 - k_y^2}} \begin{pmatrix} k_x^m k_y \\ k_y^2 - \omega^2/c^2 \\ \pm k_y k_z^m \end{pmatrix}, \quad (3)$$

$$\mathbf{e}_{m\pm}^H(k_x, k_y, \omega) = \frac{1}{\sqrt{\omega^2/c^2 - k_y^2}} \begin{pmatrix} \mp k_z^{m\pm} \\ 0 \\ k_x^m \end{pmatrix}. \quad (4)$$

The latter are chosen such that the  $y$ -components of the electric/magnetic fields vanish for  $\sigma = H, E$ . The Rayleigh reflection coefficients  $R_{mn}^{\sigma\sigma'}(k_x, k_y, \omega)$  are calculated by numerically integrating the Maxwell equations within the grating ( $0 < z < h$ ) and imposing conditions of continuity at its upper (free-space) and lower (sapphire) boundaries [2]. They are even functions of  $k_y$  and obey the following symmetries:  $R_{mn}^{\sigma\sigma'}(k_x, k_y, i\xi) = \pm R_{-m-n}^{\sigma\sigma'*}(-k_x, k_y, i\xi)$  and  $R_{mn}^{\sigma\sigma'}(k_x, k_y, i\xi) k_z^{n-} = \pm R_{-n-m}^{\sigma\sigma'*}(k_x, k_y, i\xi) k_z^{m+}$  with  $+$  for  $\sigma\sigma' = EE, HH$  and  $-$  otherwise. Our theory is able to allow for anisotropic atoms or molecules. For a sufficiently anisotropic molecule, we find a repulsive CP potential along the  $z$ -axis similar to the repulsive Casimir force predicted in Ref. [4] (see also [5]). Note that for the isotropic atoms used in the current experiment,  $\boldsymbol{\alpha} = \alpha \mathbf{I}$  ( $\mathbf{I}$ : unit tensor), Eq. (1) simplifies to Eq. (1) of the main manuscript and our formalism reduces to that of Ref. [3].

The evanescent-wave potential is generated by an incoming wave of (free-space) wavelength  $\lambda = 765$  nm which impinges on the sapphire-grating interface at an incidence angle  $\theta = 35.50^\circ = 0.6196$  rad, with the plane of incidence being parallel to the grating bars. The components of the wave vector in the sapphire layer are hence  $k_x^m = 0$ ,  $k_y = k \sin \theta = 8.39 \times 10^6 \text{ m}^{-1}$ ,  $k_z^{0+} = k \cos \theta = 1.18 \times 10^7 \text{ m}^{-1}$  ( $k = \text{Re } n_{\text{sapp}} \omega/c$  with  $\text{Re } n_{\text{sapp}} = 1.76$  and  $\omega = 2\pi c/\lambda = 2.46 \times 10^{15} \text{ rad/s}$ ). The incoming field is polarised such that its component perpendicular to the grating vanishes; it can hence be written as  $\mathbf{E}_{\text{in}}(\mathbf{r}) = E_{\text{sapp}} \mathbf{e}_{0+}^E(0, k_y, \omega) e^{i(k_y y + k_z^{0+} z)}$ . The field amplitude inside sapphire can be related to the respective laser power  $P_{\text{sapp}}$  and beam waist  $w_{\text{sapp}}$  via  $\frac{1}{2} \varepsilon_0 n_{\text{sapp}} c E_{\text{sapp}}^2 = I_{\text{sapp}} = P_{\text{sapp}}/(2\pi w_{\text{sapp}}^2)$ . The laser power is in turn related to its free-space value by  $P_{\text{sapp}} = T_{\text{free-space} \rightarrow \text{sapp}} P_{\text{free-space}}$  where  $T_{\text{free-space} \rightarrow \text{sapp}}^2 = 0.78$  has been determined experimentally from a set-up with symmetric light paths. The measured beam waist of  $170 \mu\text{m}$  in free space results in an effective beam waist  $w_{\text{sapp}} = 182.9 \mu\text{m}$  in sapphire after transitions through the free-space-glass and glass-sapphire interfaces. After transmission through the grating, the external laser leads to a field

$$\mathbf{E}(\mathbf{r}) = E_{\text{sapp}} \sum_{n=-\infty}^{\infty} \sum_{\sigma=E,H} e^{i(nq x + k_y y) - \kappa_z^{n+} z} \mathbf{e}_{n+}^{\sigma}(nq, k_y, \omega) T_{n0}^{\sigma E}(0, k_y, \omega) \quad (5)$$

with  $\kappa_z^{n+} = \sqrt{k_y^2 - \omega^2/c^2 + n^2q^2}$  where the Rayleigh transmission coefficients  $T_{mn}^{\sigma\sigma'}(k_x, k_y, \omega)$  are found from numerical integration. When interacting with a Rb atom, this evanescent field generates an optical potential

$$U_{\text{EW}}(\mathbf{r}) = \sum_{i=1,2} \frac{|\mathbf{d}_i|^2 |\mathbf{E}(\mathbf{r})|^2}{3\hbar\Delta_i} = \sum_{i=1,2} \frac{|\mathbf{d}_i|^2 E_{\text{sapp}}^2}{3\hbar\Delta_i} \sum_{m,n=-\infty}^{\infty} \sum_{\sigma,\sigma'=E,H} e^{i(m-n)qx - (\kappa_z^{m+} + \kappa_z^{n+*})z} \times e_{m+}^{\sigma}(mq, k_y, \omega) \cdot e_{n+}^{\sigma'*}(nq, k_y, \omega) T_{m0}^{\sigma E}(0, k_y, \omega) T_{n0}^{\sigma' E*}(0, k_y, \omega), \quad (6)$$

$\omega_1 = 2.37 \times 10^{15}$  rad/s,  $\omega_2 = 2.41 \times 10^{15}$  rad/s,  $d_1 = 2.54 \times 10^{-29}$  Cm and  $d_2 = 3.58 \times 10^{-29}$  Cm are the transition frequencies and dipole-matrix elements for the  $D_1$  ( $5^2S_{1/2} \rightarrow 5^2P_{1/2}$ ) and  $D_2$  ( $5^2S_{1/2} \rightarrow 5^2P_{3/2}$ ) lines of the isotropic Rb atom [6].

A numerical error in the evaluation of the potential is 0.1%. The number of Rayleigh coefficients used was selected to obtain the needed accuracy,  $N=30$  ( $2N+1$  terms in every Rayleigh expansion) is sufficient to obtain the potential with needed accuracy even at closest separations from the grating shown on Fig.2.

## II. CASIMIR-POLDER POTENTIAL USING THE HAMAKER APPROACH

The scattering Green tensor  $\mathbf{G}^{(1)}(\mathbf{r}, \mathbf{r}, \omega)$  in Eq. (1) can be expanded in a Born series with respect to a known reference Green tensor  $\mathbf{G}^{(0)}(\mathbf{r}, \mathbf{r}, \omega)$  as [7]

$$\mathbf{G}^{(1)}(\mathbf{r}, \mathbf{r}, \omega) = \frac{\omega^2}{c^2} \int d^3s \mathbf{G}^{(0)}(\mathbf{r}, \mathbf{s}, \omega) \delta\epsilon(\omega) \mathbf{G}^{(0)}(\mathbf{s}, \mathbf{r}, \omega) + \left(\frac{\omega^2}{c^2}\right)^2 \int d^3s d^3s' \mathbf{G}^{(0)}(\mathbf{r}, \mathbf{s}, \omega) \delta\epsilon(\omega) \mathbf{G}^{(0)}(\mathbf{s}, \mathbf{s}', \omega) \delta\epsilon(\omega) \mathbf{G}^{(0)}(\mathbf{s}', \mathbf{r}, \omega) + \dots \quad (7)$$

where the integration range covers the volume of the material under investigation. The perturbation  $\delta\epsilon(\omega) = \epsilon^{(1)}(\omega) - \epsilon^{(0)}(\omega)$  denotes the deviation from the reference permittivity. In the case of the free-space Green tensor as our reference, the difference permittivity simply equals the susceptibility [here:  $\delta\epsilon(\omega) = \chi_{\text{Au}}(\omega)$ ] of the material. The free-space Green tensor can be written as [7]

$$\mathbf{G}^{(0)}(\boldsymbol{\rho}, \omega) = -\frac{c^2}{3\omega^2} \boldsymbol{\delta}(\boldsymbol{\rho}) + \frac{\omega}{4\pi c} \left[ f\left(\frac{c}{\omega\rho}\right) \mathbf{I} - g\left(\frac{c}{\omega\rho}\right) \frac{\boldsymbol{\rho} \otimes \boldsymbol{\rho}}{\rho^2} \right] e^{i\omega\rho/c} \quad (8)$$

with  $f(x) = x + ix^2 - x^3$  and  $g(x) = x + 3ix^2 - 3x^3$ .

The Hamaker approach only uses the first term of the Born series expansion. Because the Born series is a perturbative expansion in the susceptibility  $\chi(\omega)$ , it converges badly for materials with a large susceptibility such as gold. To improve this convergence, and to implement a local-field correction, the reference Green tensor is separated into a regular  $\mathbf{R}$  and a singular part  $\mathbf{D} = -\frac{c^2}{3\omega^2} \boldsymbol{\delta}(\boldsymbol{\rho})$ . Inserted into Eq. (7) and performing the integrals over the  $\delta$ -distributions yields the local-field corrected first-order scattering Green tensor

$$\mathbf{G}^{(1)}(\mathbf{r}, \mathbf{r}, \omega) = \frac{\omega^2}{c^2} \chi(\omega) \sum_{n=0}^{\infty} \left(-\frac{1}{3} \chi(\omega)\right)^n \int d^3s \mathbf{R}^{(0)}(\mathbf{r}, \mathbf{s}, \omega) \mathbf{R}^{(0)}(\mathbf{s}, \mathbf{r}, \omega), \quad (9)$$

which leads to

$$\mathbf{G}^{(1)}(\boldsymbol{\rho}, \omega) = \frac{\omega^2}{c^2} \frac{\chi(\omega)}{1 + \chi(\omega)/3} \int d^3s \mathbf{R}^{(0)}(\mathbf{r}, \mathbf{s}, \omega) \mathbf{R}^{(0)}(\mathbf{s}, \mathbf{r}, \omega) \quad (10)$$

with

$$\mathbf{R}^{(0)}(\boldsymbol{\rho}, \omega) = \frac{\omega}{4\pi c} \left[ f\left(\frac{c}{\omega\rho}\right) \mathbf{I} - g\left(\frac{c}{\omega\rho}\right) \frac{\boldsymbol{\rho} \otimes \boldsymbol{\rho}}{\rho^2} \right] e^{i\omega\rho/c}. \quad (11)$$

Eq. (10) has to be evaluated numerically. Because of the smooth shape of the potential, numerical integration methods converge quickly with errors proportional to at most the curvature of the potential, which is small in the range of investigation.

In the Hamaker approach (pairwise summation) the potential is clearly additive. The total potential can be separated into three parts: one related to the evanescent field, one related to the dispersion interaction between Rb and Au, and one part for the Casimir-Polder interaction between the Rb atoms and the sapphire substrate. The latter can be neglected, because of the vastly different susceptibilities of gold and sapphire.

### III. BEC PREPARATION

The BEC is prepared in an ultra-high vacuum chamber. After precooling and trapping  $^{87}\text{Rb}$  atoms in a magneto-optic trap the atoms are adiabatically transferred into a highly compressed magnetic trap, where they are further cooled by forced radio-frequency evaporation by which Bose-Einstein condensates with typically  $2 \times 10^5$  atoms are generated. This is done at a distance of several hundred  $\mu\text{m}$  from the surface of a dielectric glass prism. A thin sapphire substrate containing the gold grating investigated in this paper is glued to the top of this prism. After preparation of the BEC we suddenly displace the magnetic trapping minimum by a distance  $\Delta z$  raising thereby the potential energy of the BEC by  $\Delta E = \frac{1}{2}m\omega\Delta z^2$  with atomic mass  $m$  and magnetic trapping frequency  $\omega$ . The BEC is accelerated towards the new trapping minimum. After a quarter of the oscillation period  $\delta t = \frac{\pi}{2\omega}$  we switch-off the magnetic trap and apply a constant magnetic field gradient of  $B' = 15 \text{ Gcm}^{-1}$  which compensates the gravitational force. Thus, the atoms are not further accelerated or decelerated due to gravitation while moving towards the grating. We measure the actual velocity of the atoms by taking absorption images of the cloud at several time intervals of 1 ms after the acceleration.

- 
- [1] S.Y. Buhmann, L. Knöll, D.-G. Welsch, and T.D. Ho, Phys. Rev. A **70**, 052117 (2004).
  - [2] A. Lambrecht and V.N. Marachevsky, Phys. Rev. Lett. **101**, 160403 (2008).
  - [3] A.M. Contreras-Reyes, R. Guérout, P.A. Maia Neto, D.A.R. Dalvit, A. Lambrecht, and S. Reynaud, Phys. Rev. A **82**, 052517 (2010).
  - [4] M. Levin, A.P. McCauley, A.W. Rodriguez, M.T.H. Reid, and S.G. Johnson, Phys. Rev. Lett. **105**, 090403 (2010).
  - [5] K.A. Milton, E.K. Abalo, P. Parashar, N. Pourtolami, I. Brevik, and S.A. Ellingsen, Phys. Rev. A **83**, 062507 (2011);  
K.A. Milton, P. Parashar, N. Pourtolami and I. Brevik, Phys. Rev. D **85**, 025008 (2012);  
C. Eberlein and R. Zietal, Phys. Rev. A **83**, 052514 (2011).
  - [6] D.A. Steck, *Rubidium 87 D Line Data*, <http://steck.us/alkalidata> (2009).
  - [7] S. Scheel and S.Y. Buhmann, Acta Physica Slovaca **58**, 675 (2008).